Varano, E., Zhou, M., Lanham, S., Iredale, R. J., van Duijneveldt, J. S., & Hamerton, I. (2019). Developing toughened bismaleimide-clay nanocomposites: Comparing the use of platelet and rod-like nanoclays. *Reactive and Functional Polymers*, *134*, 10-21. https://doi.org/10.1016/j.reactfunctpolym.2018.10.006

Developing toughened bismaleimide-clay nanocomposites: comparing the use of platelet and rod-like nanoclays.

Enrico Varano[1], Ming Zhou[1], Samuel Lanham[1], Robert J. Iredale[1], Jeroen S. van Duijneveldt[2], and Ian Hamerton[1,]*

[1]Bristol Composites Institute (ACCIS), Department of Aerospace Engineering, School of Civil, Aerospace, and Mechanical Engineering, Queen's Building, University Walk, University of Bristol, Bristol, BS8 1TR, U.K.

[2]School of Chemistry, Cantock's Close, University of Bristol, Bristol, BS8 1TS, U.K.

KEYWORDS

Bismaleimides, rod like clays, nanocomposites, thermal properties, fracture toughness.

ABSTRACT: Rod-like sepiolite organoclays are incorporated into a simple, first-generation commercial bismaleimide (BMI) to improve the inherent brittleness of the cured polymer; montmorillonite clay is used as a baseline comparison. Both solution and solid state blending methods are evaluated to determine which offer the best method of dispersion. Increased Pangel B40 (sepiolite) loading leads to finer particle sizes and a narrower size distribution indicating that the nanoclay assists the grinding and particle size refinement. The cured nanocomposites containing sepiolite nanoclays offer superior storage modulus to the montmorillonite. Introduction of Pangel B40 achieves around a 15-42% increase in plane-strain fracture toughness (depending on loading) and modest increases (+2 %) in char yield when compared with the unmodified BMI.

Introduction

Following a comparatively quiet decade during the 1990s, there has been a resurgence of interest in bismaleimides (BMIs) from both a scientific and a technical perspective as a result of their good mechanical performance, high glass transition temperature (T_g), high thermal stability, and moisture resistance, when compared with the ubiquitous epoxy resin [1]. The principal drawback of cured BMIs is undoubtedly their inherent brittleness, and a number of approaches have been explored to address this, including blending flexible monomers, such as benzoxazines [2], epoxy resins [3], and cyanate esters [4,5]. Liquid elastomers have become increasingly popular in BMI toughening, particularly carboxyl-terminated butadiene-acrylonitrile (CTBN) species bearing a terminal carboxyl group. The fracture toughness, plastic elongation, and impact strength of the toughened BMI are greatly improved. In 1987, Driscoll and Walton [6] reported that a blend of Compimide 453 with CTBN served to increase both flexibility and thermal stability, although the penalty of reduced T_g and raw material cost limit its wider use. Since the 1990s, thermoplastic reinforced BMI resins with good toughness and thermal stability have attracted considerable attention [7] and resin toughening has typically involved polyether sulfone, polybenzimidazole, or polyetherimide. Allyl modified BMI commercial products, particularly those involving diallyl bisphenol A and allylphenol [8], show good performance under hot-wet conditions (a good example is Matrimid 5292). The initial curing mechanism has been found to involve an ene-addition occurring between the allyl (diene) and the C=C in the imide ring (dieneophile).

Nanomaterials, particularly clays, have high specific surface areas and lead to substantial interaction interfaces when combined with polymer matrices and these are becoming increasingly explored. With the addition of an appropriate loading, nanofillers can generate more

microcracks and plastic deformation than common polymer materials and, when subjected to impact, the nanocomposites absorb more energy and improve the matrix toughness. Current commercial BMI products tend to use well-dispersed nanofillers [9] in consideration of the toughening effects and the cost [10]. However, to further develop the application of nanocomposites, there are a few challenges that need to be addressed: (1) the irregular dispersion state of the inorganic phase; (2) challenges in morphology control of the inorganic inclusion; (3) the low degree of interfacial reaction.

Clay/polymer nanocomposites have increasingly attracted attention from both engineering and scientific quarters. This growing interest arises from their ability to become integrated with polymer matrices and confer significant performance enhancements. A relatively small amount of nanoclay (typically < 5 wt%) can bring significant improvements not only in the mechanical properties of polymer materials [11,12], but also their barrier and thermal properties [13] and even their UV resistance [14]. In the meantime, the uniform dispersion of sepiolite (at modest levels of 1 wt %) has been shown to raise T_g significantly while improving impact and flexural strength in epoxy resins by blocking the formation of bulky segments [15].

Compimide 200 (a low molecular weight, linear aspartimide) is a first generation (untoughened) BMI, related to the materials originally reported by Crivello in his seminal paper [16], and contains 4,4’-bismaleimidodiphenyl methane (BDM), derived from bis(4-aminophenyl) methane (also known as methylene dianiline, MDA). BDM is ubiquitous in the research literature and has been reported in many studies [17,18,19] and, while the presence of aromatic moieties in the building block increase thermal stability, they do not reduce brittleness or improve

processability. MDA[1] has been shown to be efficient in improving BMI toughness through a reduction in crosslink density. Kerimid 601, originally commercialised by Rhone Poulenc) [20], originally contained around 6-12 % residual free MDA and Compimide 200 is based on the same chemistry and structures but is significantly more refined with a dramatically reduced MDA content (< 0.1 %) [21].

The aim of this work is to combine a simple, first generation, commercial BMI with a variety of functionalised clays (of different particle shapes) with the intention of producing nanocomposite-reinforced systems, which display improved ultimate properties as cured materials. The use of rod-like sepiolite clays should require less time-consuming exfoliation methods to achieve optimum dispersion than layered clays (such as phyllosilicates). If this preliminary study shows promise with the rod-like clays, then this approach will be applied to more complex formulated BMIs undergoing study in house.

Experimental methods

[1] MDA is considered a potential occupational carcinogen by the US National Institute for Occupational Safety and Health and classified by the ECHA as a 'substance of very high concern' and placed on the authorisation list. The Occupational Safety and Health Administration has set a permissible exposure limit at 0.01 ppm over an eight-hour time-weighted average, and a short-term exposure limit at 0.10 ppm. NIOSH Pocket Guide to Chemical Hazards, Barsan ME (Ed). Cincinnati OH: Department of Health and Human Services, http://www.cdc.gov/niosh/npg/npg.html (Accessed April 2016).

Materials

Compimide 200 (Table 1) was supplied in powder form by Evonik Industries (Essen, Germany); the functionalised sepiolite clays (Pangel B20 and Pangel B40, with B40 having the higher polarity of the two) are both hydrous mangnesium silicates and were a gift from Tolsa (Spain), and the sodium-rich montmorillonite (Na-Montmorillonite, as SWy-2 and SWy-3, typical particle lengths range from 500 to 1500 nm and diameters from 20 to 40 nm) were supplied by Source Clays Repository. The polyisobutylene based stabiliser (SAP 230 TP) was obtained from Infineum and *N*,*N*-dimethylformamide (DMF) >99.8% was purchased from Fisher Scientific. All materials were used as received without further purification.

Formulation and curing of BMI monomer and nanocomposite blends

Two general methods were used to disperse the clays: in solution using DMF (see Supplementary material) and through grinding and formation of molten blends. The latter method produced samples for characterisation and the details of the solution blending and film formation are supplied as supplementary information.

Solid blending

Measured quantities of the SWy-3 and Pangel B20 and B40 clays were blended with the BMI monomer at different compositions (Table 1). Both the neat BMI powder and blended nanocomposites were ground using glass balls and an IKA® Ultra TURRAX® Tube Drive at 3000 rpm for 20 minutes, at 5-minute intervals.

Cure schedule

The solid blends were cured at 175 ˚C before being held isothermally for 3 hours. A post-cure temperature of 220 ˚C (3 hours) was then performed before cooling the samples at a rate of 5 K min^{-1} to room temperature.

Microscopy

Samples of fractured surfaces were analysed using a Jeol JSM-IT300 scanning electron microscope (SEM) operating at an accelerating voltage of 15 kV or a Hitachi TM3030Plus and samples were coated to a depth of 20 nm with silver (99.99%) using an Agar high resolution sputter coater, then an aluminium foil ribbon was used to create a conductive bridge from the fracture surface being examined to the bottom surface.

Fourier transfer infrared (FTIR) spectroscopy

The BMI monomer and its blends with the nanoclays were analysed (16 scans at a resolution of 40 cm^{-1}) using a Perkin Elmer Spectrum Two FTIR spectrometer with a UATR Two attenuated total reflectance (ATR) module and analysed using OriginPro 9.0 (developed by OriginLab, USA).

Dynamic scanning calorimetry (DSC)

DSC experiments were performed using a TA Q200 calorimeter. Hermetically sealed T_{zero} aluminium pans were used, with sample masses (5 ± 0.50 mg). Analyses were conducted between 35-300 °C, at a heating rate of 5 K min^{-1}, with the sample cell kept under a constant nitrogen flow of 50 cm^3 min^{-1}. Melting points, curing temperatures, and glass transition temperatures were taken as the middle point of the transition.

Thermogravimetric analysis (TGA)

TGA measurements were performed on samples (30 mg) using a TA Instruments TGA Q500 instrument equipped with alumina sample pans. Experiments were undertaken on cured nanocomposite samples in an inert environment (nitrogen, 50 cm^3 min^{-1}) at a heating rate of 10 K min^{-1}.

Dynamic mechanical thermal analysis (DMTA)

DMTA measurements were performed using a TA Instruments DMA Q800 instrument equipped with a single cantilever bending (SCB) fixture. A heating rate of 5 K min^{-1} and displacement amplitude of 15 μm were used throughout. The DMTA test samples were manufactured by curing the ground powders in round aluminium pans (diameter 50 mm) according to the cure schedule. The round plates were extracted from the pans, cut using a diamond-tipped saw and sanded to yield regular rectangular samples dimensions averaging 40 × 13 × 5 mm^3 as required by the SCB fixture manual (the recommended dimensions for the SCB samples were 35 × 12 × 3 mm^3).

Mechanical Testing

To create the rest of the test samples, a two-part, steel mould held together by bolts and having inner dimensions of 20 × 65 × 105 mm^3 was used. The chosen test method followed the ASTM D5045-14 standard for a single edge notched beam (SENB) test [22]. The cured resin blocks were cut into samples (52.3 – 53.5 mm long, 11.8-12.6 mm wide, 5.5 – 6.3 mm thick), using a diamond-tipped saw and sanded to yield regular rectangular samples, which conformed to the ratio of dimensions required by the standard. The initial notch was cut using a diamond tipped

saw and widened using a hacksaw. To initiate a crack in the SENB specimen, a new razor blade was tapped into the material with a small hammer. Each sample was loaded into the test machine (Supplementary Fig. S2). Mechanical testing was conducted using an Instron 3343 Universal testing machine with a 1 kN load cell and a displacement rate of 10 mm min^{-1}.

Once the testing was complete, the crack depth was measured on both parts of each failed specimen in three locations. This was done in order to get an average value of the crack depth within each specimen for the fracture toughness calculation, the equation for which is shown below (1).

$$K_{Ic} = \frac{P_q}{BW^{0.5}} f(x) \qquad (1)$$

where *B* is the thickness, *W* is the width, *f(x)* is a function of *a/W* and P_q is the load. Details of how to find P_q are found in the D5045-14 standard. When measuring the crack length and calculating *a/W,* some of the specimens were outside the range of 0.45 to 0.55 and so these samples were discounted. It ruled out 17 of the unmodified BMI-0 samples, two of the BMI-$SWy3_{2.5b}$ samples, one of the BMI-$SWy3_{5b}$ samples, six of the BMI-$B40_{2.5b}$ samples, and five of the BMI-$B40_{5b}$ samples, which left the final results ranging from 0.45 to 0.80. It is pertinent to note that there was a smaller number of the BMI-SWy3 samples due to a limited availability of materials.

Results and discussion

Investigating the stability of the clays within the BMI

Several clays were examined during the course of the work: montmorillonite ($(Na,Ca)_{0.33}(Al,Mg)_2(Si_4O_{10})(OH)_2 \cdot nH_2O$) is a phyllosilicate that has been explored most widely

with BMIs and other high performance polymers [23,24,25,26] and was included for comparison. However, its layered structure means that careful exfoliation is required to achieve desirable final cured polymer properties. In contrast, sepiolite ($Mg_4Si_6O_{15}(OH)_2 \cdot 6H_2O$) is a novel material in the context of BMI chemistry. It is a rod-shaped, mineral clay consisting of an octahedral magnesium layer sandwiched between two silica tetrahedral layers [27]. The organoclays used here (Pangel B20 and B40) are modified by adsorbing quaternary ammonium surfactants to the particle surface. They are commonly used as viscosity modifiers, with the B20 grade designed for intermediate polarity systems and B40 for high polarity systems. The sepiolite nanoparticles have high aspect ratios (particle lengths range from 500 to 1500 nm and diameters from 20 to 40 nm – [28]) and are characterised by porous channels (3.6 Å x 10.6 Å), which are oriented along the particle's length, and can absorb water and some organic monomers [29].

The use of aprotic solvents to process polyimides (and particularly BMIs) is commonplace. Thus, in traditional BMI systems, either high temperatures (>150 °C) or high-boiling solvents (*e.g. N*,*N*-dimethylformamide, *N*-methylpyrrolidone and *N*,*N*-dimethylacetamide – DMF, NMP, and DMAc respectively) are required in order to allow the fabrication of composite products. However, the use of such solvents can present challenges with solvent removal especially when a strongly solvating compound, such as DMF, is used. An additional epoxy component may be added to aid processing by improving flow properties, but this ultimately detracts from the thermal, electrical, and mechanical performance of the BMI resin [30] and consequently this approach was not employed in this work. While DMF is highly efficient for solvation, the effects of residual solvent on polymerization behaviour may be profound. Hamerton *et al.* [31] reported a series of BMI-terminated aromatic polyaspartimides based on two and four-ring moieties and compared the merits of solution and molten blending methods. They reported that the effect of

residual DMF reduced the onset of thermal degradation by 20-60 °C in cured polyaspartimides prepared using a molten blend route, and so solvent removal is key to success.

Despite the suspected difficulties in removing the DMF, it was deemed worthwhile to investigate the compatibility of the BMI and clays in solution as this approach allowed for more controlled mixing and therefore even clay exfoliation. This preliminary work was ultimately unsuccessful, but the data have been included as supplementary information. The work carried out on the BMI and clays within DMF indicated that there was better affinity between the BMI molecules and the sepiolite nanoparticles coated with polar surfactants (Pangel B40 in particular) than traditionally investigated BMI-montmorillonite systems. However, to overcome the issues faced in removing the solvent before cure, an alternative solid-blending process was investigated. Three solid mix samples (BMI-$B40_{2.5b}$ and BMI-$B40_{5b}$ containing 2.5 and 5 wt% B40 respectively, and BMI-$SWy3_{2.5b}$ containing 2.5 wt% SWy3) were created in order to determine the relative effect of different fractions of the sepiolite organoclay on the thermo-mechanical properties, and to compare some measurements to the montmorillonite doped samples. The principal concern was whether the solid-state method would achieve an acceptable level of dispersion and optical microscopy was used with visualisation under plane-polarised light to analyse the morphologies of the monomer/clay blends. There was no obvious aggregation or crystal twinning observed in three samples (Fig. 1 (a), (b), and (c)) under polarized light. The results from the optical microscopy are consistent with the particle size dispersion analysis from the same samples (Fig. 1 (d), (e), and (f)). Interestingly, finer particle sizes were observed with increasing loading of sepiolite Pangel B40 nanoclay with a larger contribution from 3-4 μm particles in the composition along with a narrowing in the distribution peak, which indicates a

potential for better incorporation. This suggests that the nanoclay may have played a role in assisting the grinding and resulted in the refinement of the particle sizes.

Investigating the thermal behaviour of the clay-BMI blends

The thermal behaviour was examined using dynamic DSC experiments and the resulting data for seven samples (the BMI monomer and monomer/clay blends with each clay in two different concentrations) prepared using the solid-state technique are shown in Table 2 and Fig. 2.

All samples demonstrate similar behaviour: a narrow melting transition occurs at around 80 °C followed by a broad melting transition at around 130 °C, which precedes a rapid onset of polymodal polymerisation exotherm (with T_{max} 200 °C), representing several reactions and spanning 140-300 °C. Owing to the proximity of the double bond in the maleimide ring to two carbonyl groups, the BMI is highly activated towards thermally-induced polymerization *via* a free radical mechanism and once the monomer becomes molten the reaction proceeds rapidly. Quantification of the DSC exotherms is difficult in this case as this overlap between endothermic and exothermic responses is coupled with a steep baseline, indicating a significant difference in heat capacity for the uncured and cured blends. The addition to 2.5 and 5 wt% Pangel B40 has a subtle influence on the thermal behaviour of the BMI, leading to initiation of a lower temperature peak (*ca.* 160 °C). The proximity of the melting and polymerisation events does have implications for processing, since the polymerisation reaction occurs practically immediately after the blends become molten. This means that there is a very short processing window, which could have implications for resin degassing.

Cure monitoring using FTIR spectroscopy

The FTIR spectrum of the Compimide 200 (BMI-0), along with selected assignments for characteristic bands [32,33] are given in Supplementary Table S3. These assignments would form the basis for subsequent cure monitoring. The FTIR spectra of the prepolymer blends and nanocomposites before and after curing are shown in Supplementary Fig. S4. Of particular note are the reductions in the characteristic vibrations due to the maleimide ring (=C-H stretch at 3106 cm^{-1}, C=C stretch at 1630 cm^{-1}, and =C-H out of plane deformation at 895 cm^{-1}) following cure, with corresponding increases in saturated CH stretch at 2980 cm^{-1}.

Twelve BMI samples (each around 20 mg) were added to individual aluminium pans and heated isothermally at 160 ˚C to explore the kinetics of polymerisation during the first stage of the cure process. Samples were removed from the oven at 5-minute intervals, quenched at room temperature (20 ˚C) before being analyzed using FTIR spectroscopy; the stacked plot (Fig. 3, left) represents each stage of the cure. An expanded region of the spectrum, showing the higher frequency vibrations associated with the maleimide ring, is also shown (Fig. 3, right).

The degree of conversion (α) was calculated from equation 2.

$$\alpha = \left(1 - \frac{A\prime(3106)}{A\prime(3034)} \Big/ \frac{A(3106)}{A(3034)}\right) \times 100 \qquad (2)$$

where A'_{3106} = absorbance intensity of =C-H stretch at 3106 cm^{-1} at time t, A'_{3034} = absorbance intensity of Ar-H stretch at 3034 cm^{-1} at time t, A_{3106} = absorbance intensity of =C-H stretch at 3106 cm^{-1} at time zero, A_{3034} = absorbance intensity of Ar-H stretch at 3034 cm^{-1} at time zero.

The selection of the frequencies to be monitored were based on the premise that the maleimide ring (=C-H stretch) will be consumed as the free radical polymerisation proceeds, while the aryl C-H stretches will be largely unaffected as they do not participate in the reaction (and thus

provide an internal standard). Thus, A' represents the absorption peak area of polymer, and A is the peak area of monomer. The progress in the degree of conversion for the maleimide as a function of time (Fig. 4) shows that following a rapid consumption of maleimide groups to form oligomers (*ca.* 15 % of the groups have undergone reaction after 10 minutes), the rate of reaction begins to slow and the blend tends to vitrify at a conversion of 25 % after 55 minutes.

This compares well with spectral data reported for the structurally similar BMI, Kerimid 601 [33], although the Michael addition of the amine to the maleimide ring is significantly faster [34,35]. The reaction efficiency of the maleimide group is related to the final curing temperature, and an increase in reaction temperature will induce a higher degree of cure. This confirms the case for a second higher temperature step to increase molecular mobility and facilitate crosslinking.

Properties of cured BMI blends and nanocomposites

Following the application of higher temperature cure steps (180 °C for 1 hour and 200 °C for 30 minutes), the cured samples were analysed using dynamic mechanical thermal analysis (DMTA). Preliminary thermogram data also demonstrate that the nanocomposites are incompletely cured through the increase in the plot beyond the rubbery modulus (which may also reflect the increased mobility of the sepiolite clay beyond T_g), yet the addition of the sepiolite nanoclay still has a significant effect on the stiffness of the cured BMI in this region, compared to the SWy-2 clay (Supplementary Fig. S7). Unfortunately, the unmodified (BMI-0) samples were too brittle to allow DMTA analysis to be conducted, so only comparison to the 'baseline' SWy-2 sample was possible and selected data points from further testing are presented in Supplementary Table

S4. The marked increase in storage modulus above 200°C gained through the addition of the B40 sepiolite can be seen (Fig. 5) even in the partially cured BMI samples.

The implementation of a second, more severe cure schedule (with 3-hour periods at both the lower temperature and the post cure temperature) ultimately yielded T_g values of 240-251 °C (from the DSC rescan experiments, Table 2) and these samples were taken forward to further thermal and mechanical testing. The thermal stability of the cured BMI species containing B40 were assessed using TGA and the mass loss data are shown for all three species (Fig. 6). It is apparent that the degradation mechanism proceeds in three steps, corresponding to single bond scissions (rate of mass loss, 0.16% $°C^{-1}$), degradation of aromatic rings (rate of mass loss, 0.5% $°C^{-1}$), and char formation (rate of mass loss, 0.14% $°C^{-1}$). The inclusion of the clay at this level has little influence on the first two stages of the mechanism, thus the BMI retains its thermal stability, but results in an increase in the char yield (the residual mass at 800 °C) of around 2%, probably reflecting the addition of clay (2 wt %).

Fracture Mechanics of cured BMI nanocomposites

Only the most promising samples (using sepiolite Pangel B40), based on the foregoing measurements, were taken forward for fracture mechanics analysis. The samples were tested following thermal cure under both schedules using the ASTM D5045-14 standard for a single edge notched beam (SENB) test. Owing to the brittle nature of the cured resins, this is a challenging task - to create a crack in the more brittle samples without destroying them, since the crack is initiated by striking a razor blade at the apex of the notch using a mallet. Consequently, many samples were lost during the crack initiation stage (*e.g.* loss of 17/23 samples for BMI-0).

In accordance with the ASTM standard method, if a crack cannot be started due to the brittleness of the material, then a scratch should be made instead. This means that for more brittle samples, a higher amount of energy is expended to create a crack, instead of just propagating it. This has the unintended consequence of causing brittle samples to register higher values than intended for the trial plane-strain fracture toughness, K_Q. This in turn explains the wider ranges observed for neat BMI-0 samples (Table 3) and for the lower clay loadings recorded later for the more highly cured samples (discussed later).

The force/displacement data (Table 3) are displayed for BMI nanocomposites containing sepiolite Pangel B40 and the fracture toughness for each sample was calculated from the force/displacement data. The mechanical data from the SENB samples shows that the incorporation of sepiolite Pangel B40 results in an increase in fracture energy. Moreover, the incorporation of 5 wt% Pangel B40 results in a two-fold increase over the 2.5 wt% Pangel B40 samples. The reduction in the scatter of the data (Table 3) reflects the results of toughening since fewer samples are lost during crack initiation but before measurement (*e.g.* 5/11 for BMI-$B40_{5b}$).

The exposed fracture surfaces were examined using SEM (Fig. 7) from which the reason for the increased toughness is clearly apparent. The fractured sample of BMI-0 shows a comparatively smooth surface (Fig.7 (a)), perhaps showing some evidence of unreacted crystalline monomer and some microvoids, diameter 40-50 μm, which promote crack formation. The presence of larger voids (80-100 μm) due to shear mixing is evident, but these do not appear to have promoted crack formation. The incorporation of sepiolite Pangel B40 produces increasingly complex topography.

The exposed fracture surfaces were further analysed using energy dispersive X-ray (EDX) spectroscopy (Fig. 8), from which the distribution of the sepiolite Pangel B40 clay in the cured nanocomposites could be determined. The larger aggregates (15-40 μm) are clearly visible, but these make a comparatively small contribution to the composition and the presence of a great number of 4 μm particles in the BMI-B40$_{5b}$ may be more significant in the complex fracture surfaces (Fig. 7 (e) and (f)). Future work will be undertaken to improve the homogeneity of this dispersion.

Another set of samples were analysed following exposure to the second, more severe, cure schedule (175 ˚C (3 hours) + 220 ˚C (3 hours) and the data (Fig. 9) confirm that the addition of sepiolite clay improves the fracture toughness of the BMI resin, and values of K_Q were within the expected range for a thermoset resin [36]. For B40 and SWy-3, higher loadings of nanoclay result in a reduction in K_Q, possibly due to agglomeration of clays that cause local defects and reduced matrix/reinforcement interaction [37,38]. This suggests that, for B40 and SWy-3, the weight loading that results in the largest increase in K_Q must be no greater than 5%. However, in contrast for the B20 clay, K_Q continues to increase with higher weight loadings, suggesting that the BMI pre-polymer may intercalate more successfully into the interclay regions, and on polymerization produces a more homogeneous nanocomposite [39]. It should be noted that, owing to the number of voids present in the blend samples (Fig. S8), each potentially acting as local defects, the values of K_Q obtained (Fig. 9, top), are not likely not be representative of the materials' true fracture toughness. However, the values obtained still facilitate the comparison of the materials and the effect of different varieties and weight loadings of clay on the properties of the resin. The trial critical strain energy release rate, G_Q (Fig. 9, bottom), is a further indication of toughening, as it increases as clay content is increased, due to the greater fracture surface deformations. The values for G_Q are lower than expected, due to the presence of air bubbles that reduce the effective fracture surface area; the calculations anticipate a larger fracture surface being created, which results in a lower G_Q value.

However, as all the samples exhibited a similar distribution of bubbles (*i.e.* all were equally poor), a qualitative comparison is possible. The spread of G_Q values also allows assessment of whether a crack was successfully initiated prior to testing: a particularly high G_Q value implies that a crack was not initiated, as a high amount of energy will be spent in creating a crack. The high G_Q values observed for the B40 clay indicate that a number of samples did not have a significant crack already initiated but had a small scratch as is compliant with the ASTM when a crack cannot be formed without destroying the sample. SEM was again used to analyse the fracture surfaces of the SENB samples. The fracture surface of the neat BMI-0 (Fig. S9 (a)) was largely featureless but did exhibit some scarps; the presence of excessive void content is clearly visible. The SEM images illustrate the differences between various clay types and loadings. In various samples, the effect of clay weight loading on morphology is noticeable, with several scarps visible (Fig. S9 (a)), which is characteristic of crack pinning [40]. Scarps form when cracks propagate on different planes, then converge on a single plane. These deformations are further evidence of toughening: the energy of fracture for brittle matrices is low and so there is little matrix deformation during failure [39]. A higher contrast was used to highlight riverline and scarp features (Fig. 7). Similar scarp features were observed in all toughened samples, although in the lower weight loadings (Figs. S9 (a), (c), and (e)) they were the prevalent feature, with a transition to wrenched tactoids evident at higher weight loadings (Figs. S9 (b), (d), and (f)), consistent with agglomeration. This seems to confirm the results from the SENB testing, where it was suspected that increased agglomeration was a cause of the decrease in fracture toughness.

Opelt *et al.* have suggested that the presence of these tactoids on the fracture surface indicates a crack deflection mechanism, through which the crack has propagated out of its initial plane [40]. Agglomeration also appears to occur within the BMI-B40$_{5b}$ sample, Fig. S9 (b), but less distinct phases are visible; the implication being that B40 facilitates a better dispersion within the BMI. The BMI-B20$_{5b}$ sample appears to be more homogeneous than the other two samples at this weight loading, with a generally more roughened surface characteristic of a toughened material. Analysis using a higher level of zoom (x 2000 magnification) also highlighted features characteristic of the crack pinning mechanism: features identified as parabolas [39] occur when inhomogeneities (in this case the clay nanoparticles) occur both ahead of, and in the same plane as, the crack which pins the matrix. An example of this is highlighted for BMI-B40$_{5b}$ (Fig. 10)

and was observed in all toughened samples at x 2000 magnification. Ribbons were a further deformation observed in some samples *e.g.* both B40 weight loadings (BMI-$B40_{2.5b}$ and BMI-$B40_{5b}$) and the 5% B20 weight loading (BMI-$B20_{5b}$).

Conclusions

This work has shown that rod-like sepiolite organoclays may be incorporated into a simple unformulated BMI and dispersed adequately without the need for extensive, surfactant-based exfoliation methods. Simply grinding with glass balls for a short period of time (10-20 minutes) combines the BMI monomer and the nanoclay and achieves a refinement in the particle size distribution. According to spectral data, the unmodified BMI tends to vitrify at a conversion of 25% at 160 °C, while the introduction of the clay accelerates the cure reaction. However, this particular BMI displays a very narrow processing window (with fusion directly preceding the onset of cure) as it has been chosen for structural simplicity to demonstrate the concept, rather than its rheological characteristics. The incorporation of all the nanoclays studied improves the flexural modulus of the BMI (as evidenced by DMTA), and both sepiolites are shown to be superior to the montmorillonite. The thermal stability of the BMI-sepiolite nanocomposites at relatively modest levels (2.5 and 5 wt%) is similar to that of the unmodified BMI, with modest enhancements of the char yield. Most encouraging are the data from fracture mechanics as the introduction of 2.5 and 5 wt% sepiolite Pangel B40 both achieve significant improvements in fracture energy and morphology. The introduction of sepiolite Pangel B40 achieves a 15-42% increase in plane-strain fracture toughness (depending on loading) compared with the unmodified BMI. Having established the potential of these rod-like nanoclays with a first-generation BMI, our efforts will now focus on our more processible, solvent-free, infusible BMI formulations to achieve true exfoliation and a higher loading of sepiolite.

AUTHOR INFORMATION

Corresponding Author

** Correspondence to Dr Ian Hamerton, E-mail: ian.hamerton@bristol.ac.uk*

Author Contributions

The manuscript was written through contributions of all authors. All authors have given approval to the final version of the manuscript.

ACKNOWLEDGEMENTS

This work was supported by the Engineering and Physical Sciences Research Council through the EPSRC Centre for Doctoral Training in Advanced Composites for Innovation and Science [grant number EP/L016028/1]. The authors thank Dr Tim Pohlmann and Dr Sergey Evsyukov (Evonik, Essen, Germany) for supplying the Compimide 200, and Mr M Perez (Tolsa, Spain) for the sepiolite. We thank Dr Steve Rae, Mr Ian Chorley, and Mr Desmond He (Department of Aerospace Engineering) for assistance during the laboratory experiments.

ABBREVIATIONS

ATR, attenuated total reflectance; BDM, 4,4'-bismaleimidodiphenyl methane; BMI, bismaleimide; DMAc, *N*,*N*-dimethylacetamide; DMF, *N*,*N*-dimethylformamide; DMTA, dynamic mechanical thermal analysis; DSC, differential scanning calorimetry; EDX, energy dispersive X-ray; FTIR, Fourier transform infrared; MDA, methylene dianiline or bis(4-aminophenyl) methane; NMP, *N*-methylpyrrolidone; SCB, single cantilever beam; SEM, scanning electron microscopy; SENB, single etch notched beam; TGA, thermogravimetric analysis.

Table 1. Sample designations for the solid blends studied in this work.

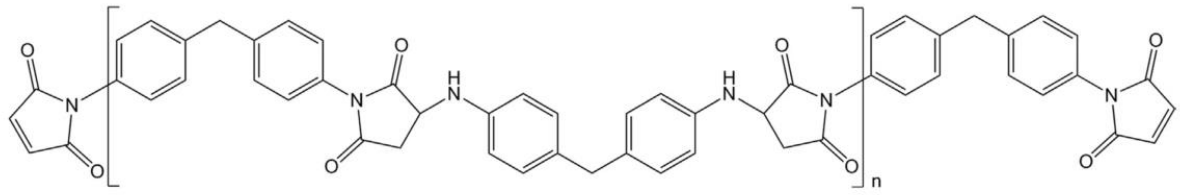

Compimide 200

Sample	Compimide 200 (wt%)	Montmorillonite	Sepiolite
		SWy-3 (wt%)	Pangel B40 (wt%)
BMI-0_b	100	-	-
BMI-$B40_{2.5b}$	97.5	-	2.5
BMI-$B40_{5b}$	95	-	5
BMI-$SWy3_{2.5b}$	97.5	2.5	-

Table 2 Thermal behaviour of Compimide 200 blends and nanocomposites from DSC data

Sample	Clay (wt %)	T_o (°C)	T_{max} (°C)	ΔH (J/g)	T_g (°C)
BMI-0	-	147	197	251	246
BMI-$B20_b$	2.5	145	215	236	251
	5.0	145	217	241	249
BMI-$B40_b$	2.5	144	194	251	237
	5.0	145	193	227	246
BMI-$SWy3_b$	2.5	145	196	233	244
	5.0	143	195	225	251

Key: T_o = onset of thermal polymerisation, T_{max} = peak maximum of exothermic peak, ΔH = polymerisation exotherm, T_g = glass transition temperature (from rescan experiment).

Table 3. Experimental fracture data for cured BMI blends from three-point bending test (SENB) with respect to three batches of cured BMI resins.

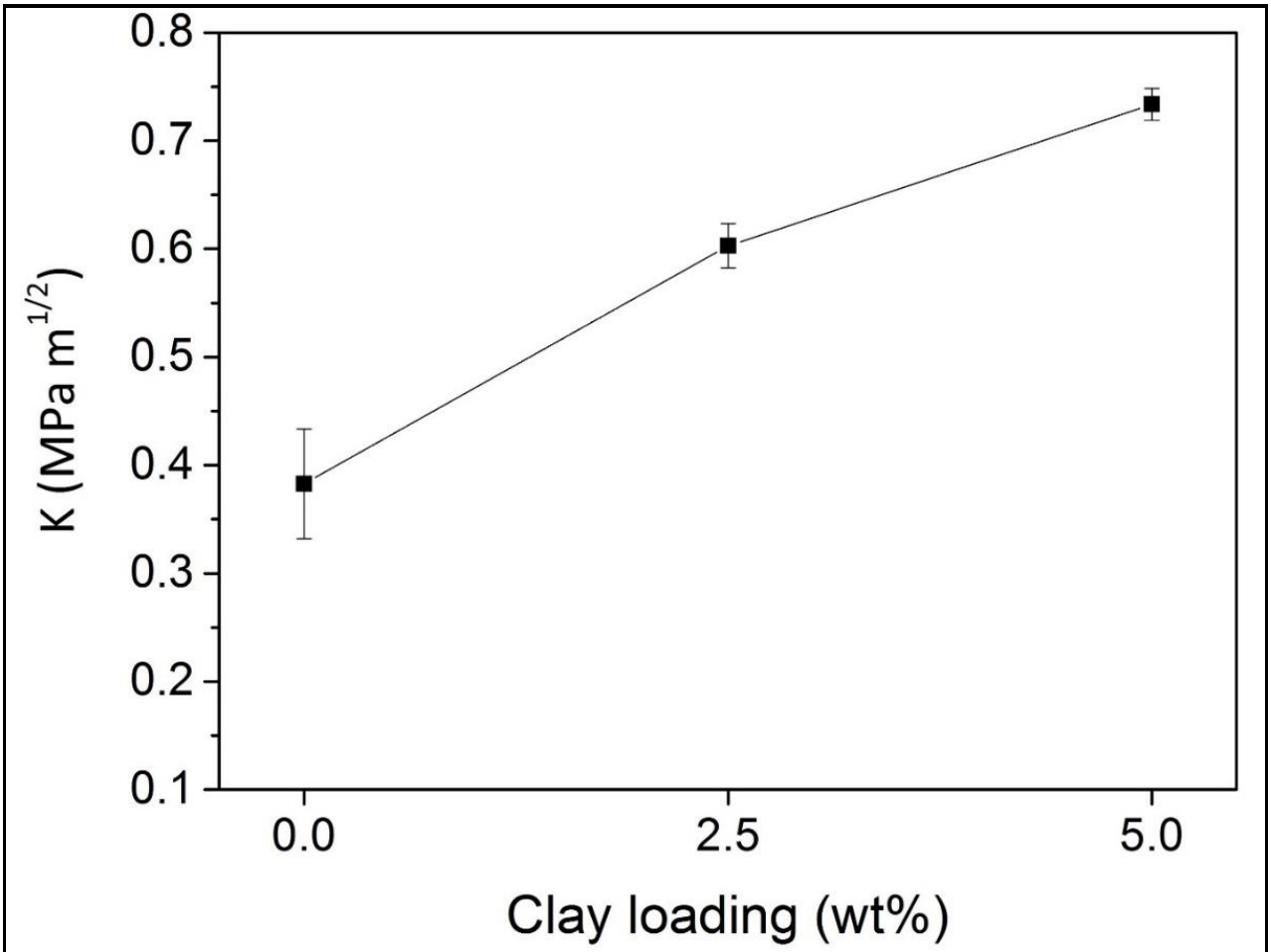

Resin		P(x) (kN)	Width (W, cm)	Crack (a, cm)	a/W	Thickness (cm)	f(x)	K_Q (MPa $m^{1/2}$)	$\overline{K_Q}$ (MPa $m^{1/2}$)
BMI-0	1	0.030	1.23	0.60	0.49	0.60	10.16	0.46	0.38
	2	0.019	1.20	0.55	0.46	0.62	9.41	0.26	
	3	0.030	1.18	0.58	0.49	0.60	10.32	0.48	
	4	0.021	1.18	0.55	0.47	0.57	9.55	0.33	
BMI-$B40_{2.5b}$	1	0.040	1.26	0.60	0.48	0.62	9.85	0.56	0.61
	2	0.040	1.19	0.55	0.46	0.57	9.41	0.60	

	3	0.036	1.24	0.60	0.48	0.60	10.00	0.54	
	4	0.047	1.22	0.57	0.51	0.56	9.55	0.72	
BMI-$B40_{5b}$	1	0.046	1.23	0.58	0.47	0.60	9.70	0.66	0.74
	2	0.050	1.19	0.55	0.46	0.55	9.41	0.78	
	3	0.044	1.18	0.55	0.47	0.58	9.55	0.63	
	4	0.051	1.22	0.65	0.53	0.63	11.74	0.86	

N.B., Critical stress intensity factor, K_Q, was calculated based on ASTM D5045-14. Each data point represents the mean of four experiments.

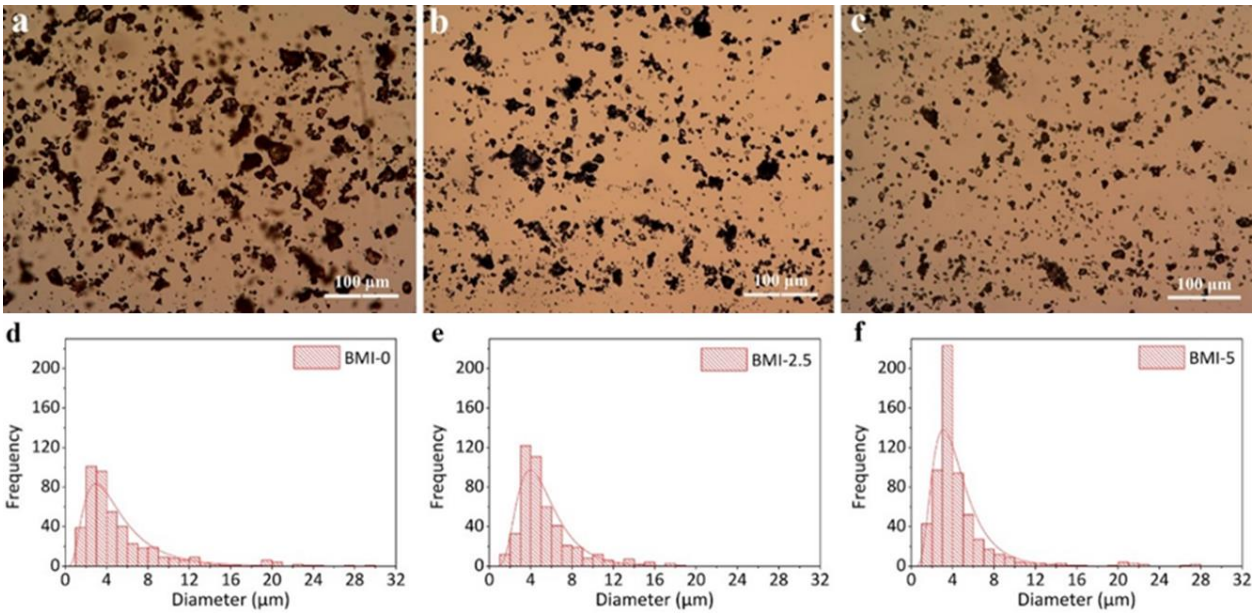

Figure 1. Optical micrographs of (a) BMI-0, and nanocomposites (b) BMI-$B40_{2.5b}$, (c) BMI-$B40_{5b}$; and their corresponding particle size dispersions: (d), (e) and (f) respectively.

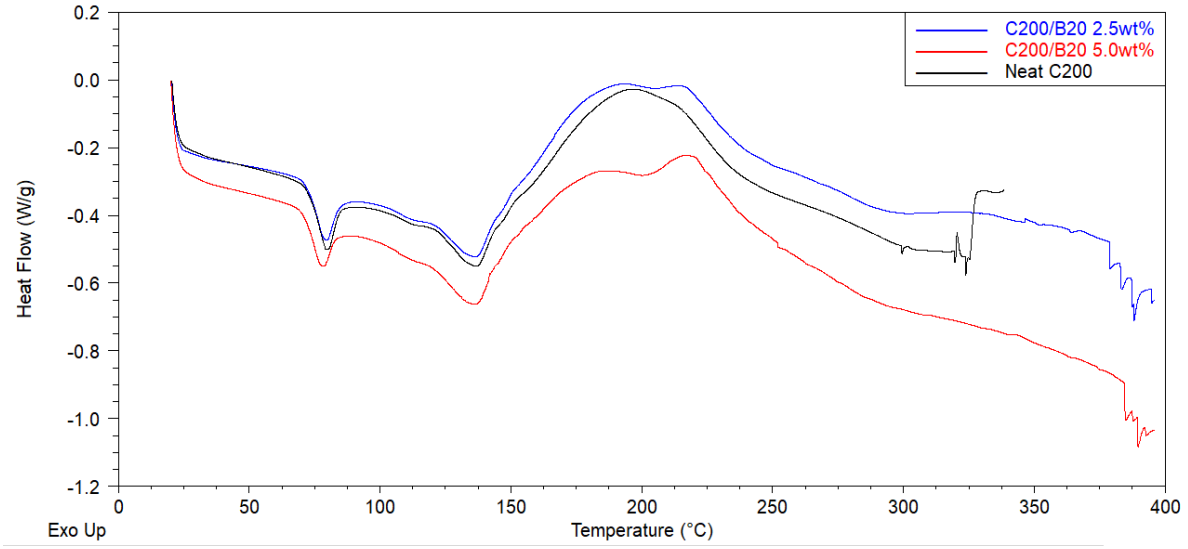
C200/B20 2.5wt%
C200/B20 5.0wt%
Neat C200
Heat Flow (W/g)
Exo Up
Temperature (°C)
0.2
0.0
-0.2
-0.4
-0.6
-0.8
-1.0
-1.2
0
50
100
150
200
250
300
350
400

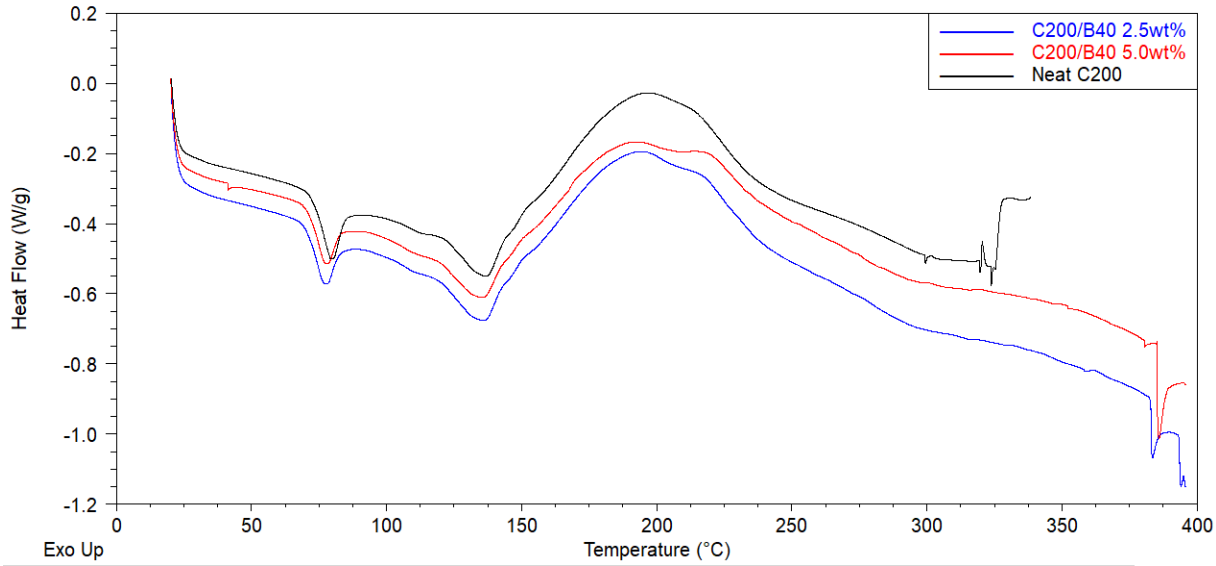
C200/B40 2.5wt%
C200/B40 5.0wt%
Neat C200
Heat Flow (W/g)
Exo Up
Temperature (°C)
0.2
0.0
-0.2
-0.4
-0.6
-0.8
-1.0
-1.2
0
50
100
150
200
250
300
350
400

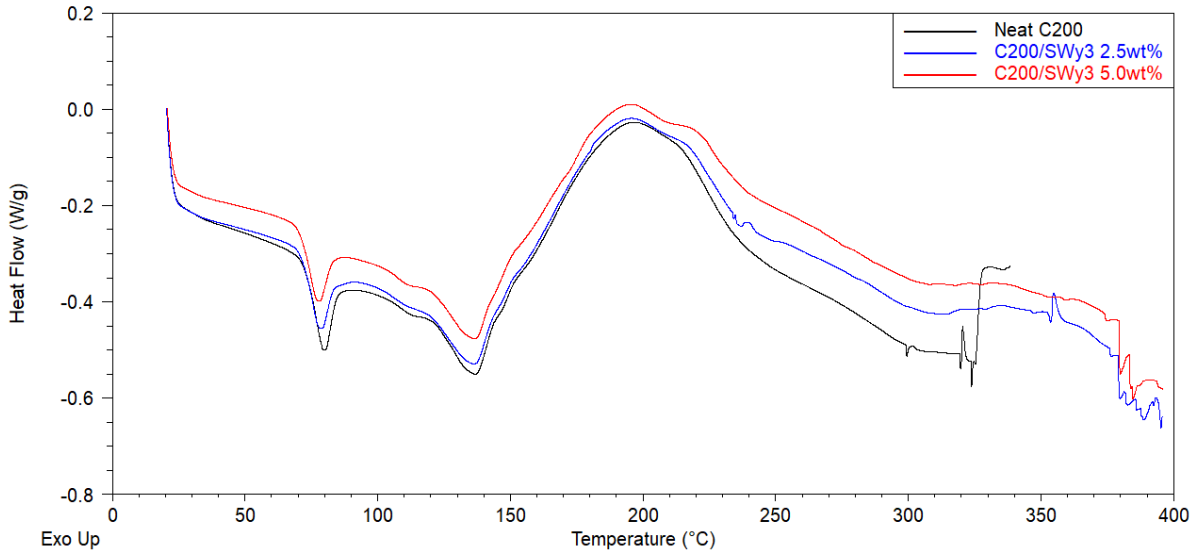

Figure 2. Differential scanning calorimetry (10 K min^{-1} under nitrogen) for uncured BMI blends (*N.B.*, C200 represents Compimide 200, BMI-0).

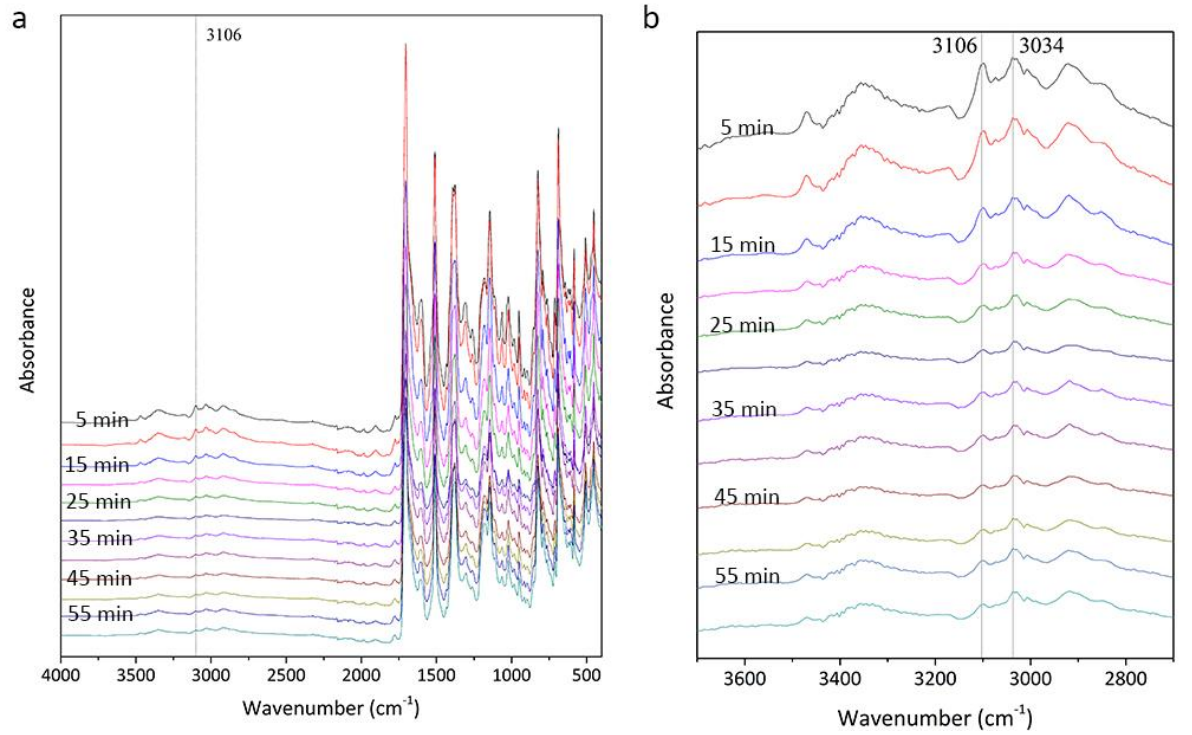

Figure 3. Stacked plot showing FTIR absorbance spectra acquired during first stage of cure with =C-H stretch (maleimide) indicated (left), inset showing expansion (right).

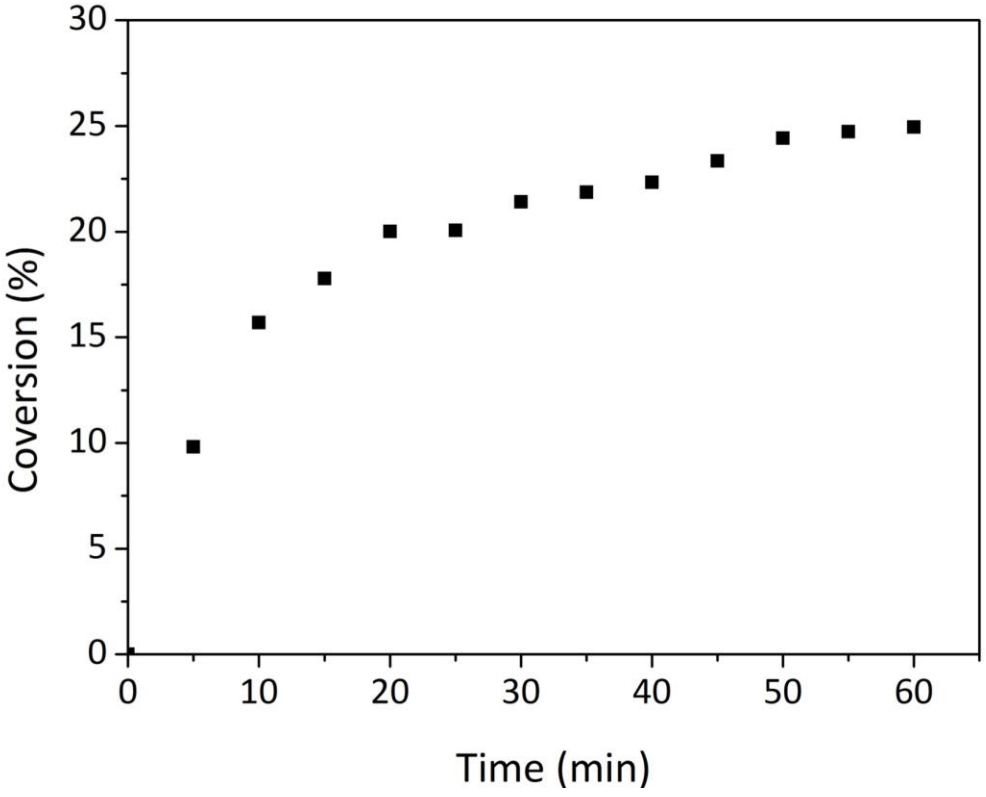

Figure 4. Fractional conversion for BMI-0 during first stage of cure (160 °C) calculated from spectral data.

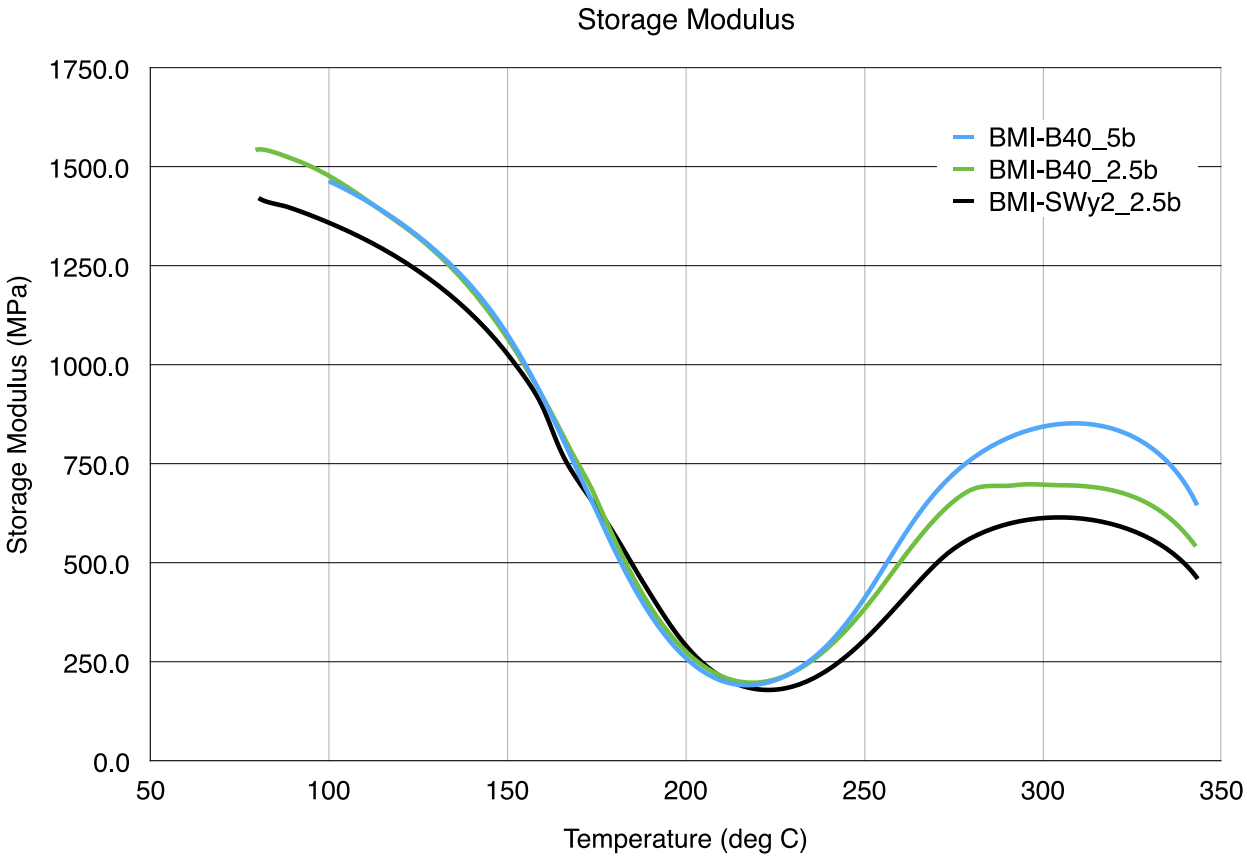

Figure 5. DMTA data (storage modulus) for BMI-SWy2$_{2.5}$ (black), BMI-B40$_{2.5b}$ (red), and BMI-B40$_{5b}$ (blue) as a function of temperature.

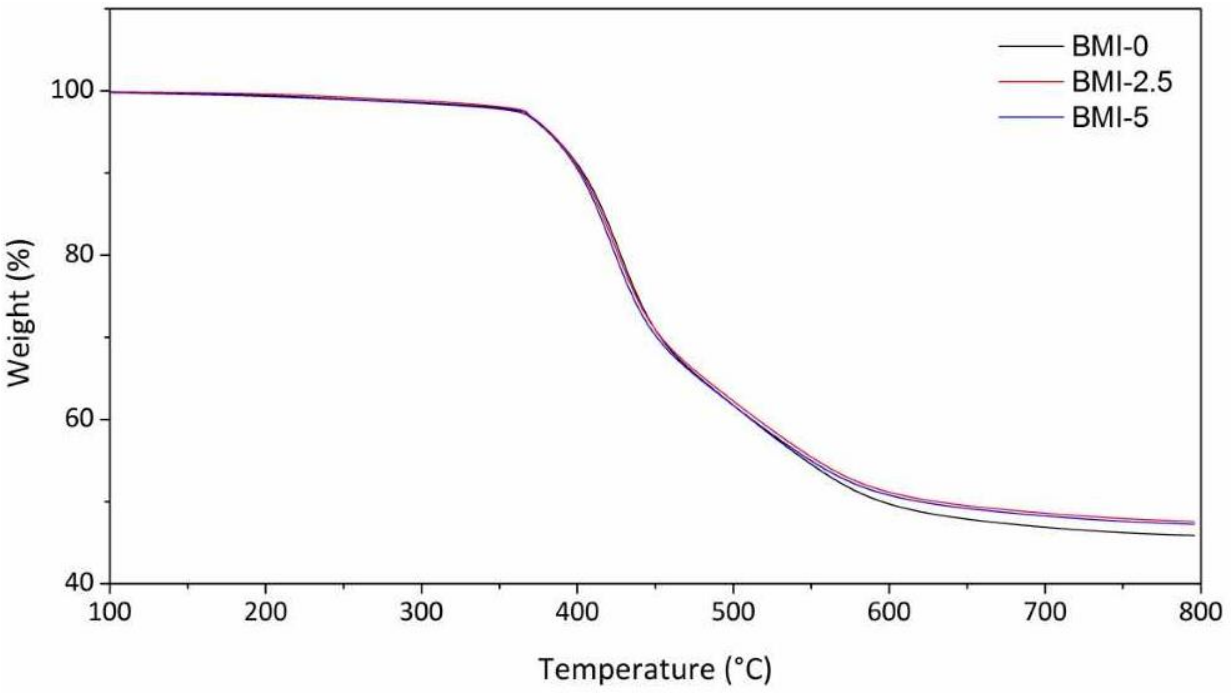

Figure 6. TGA data for cured samples of BMI-0 (black), BMI-B40$_{2.5b}$ (red), and BMI-B40$_{5b}$ (blue) as a function of temperature.

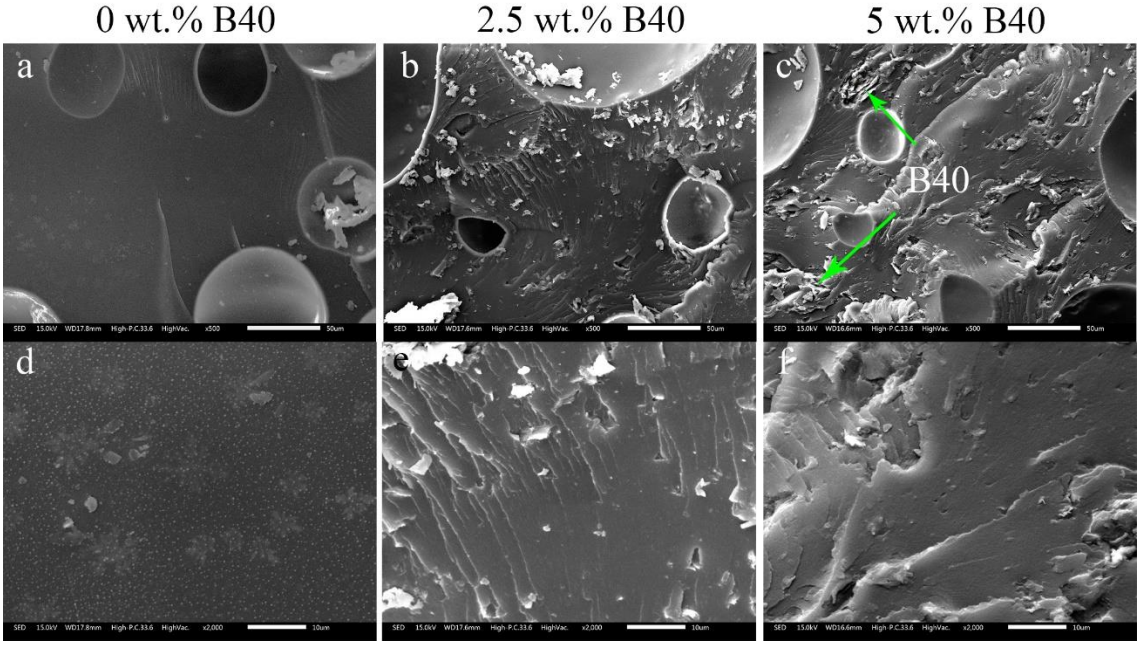

Figure 7. SEM images of fracture surfaces at different resolutions (a) BMI-0, (b) BMI-B40$_{2.5b}$, (c) BMI-B40$_{5b}$ (all 500x) and (d) BMI-0, (e) BMI-B40$_{2.5b}$, (f) BMI-B40$_{5b}$ (all 2000x, scale bar represents 50 μm (a-c) and 10 μm (d-f). Note, all samples were cured using the following schedule: 180 ˚C (1 hour) + 200 ˚C (30 minutes).

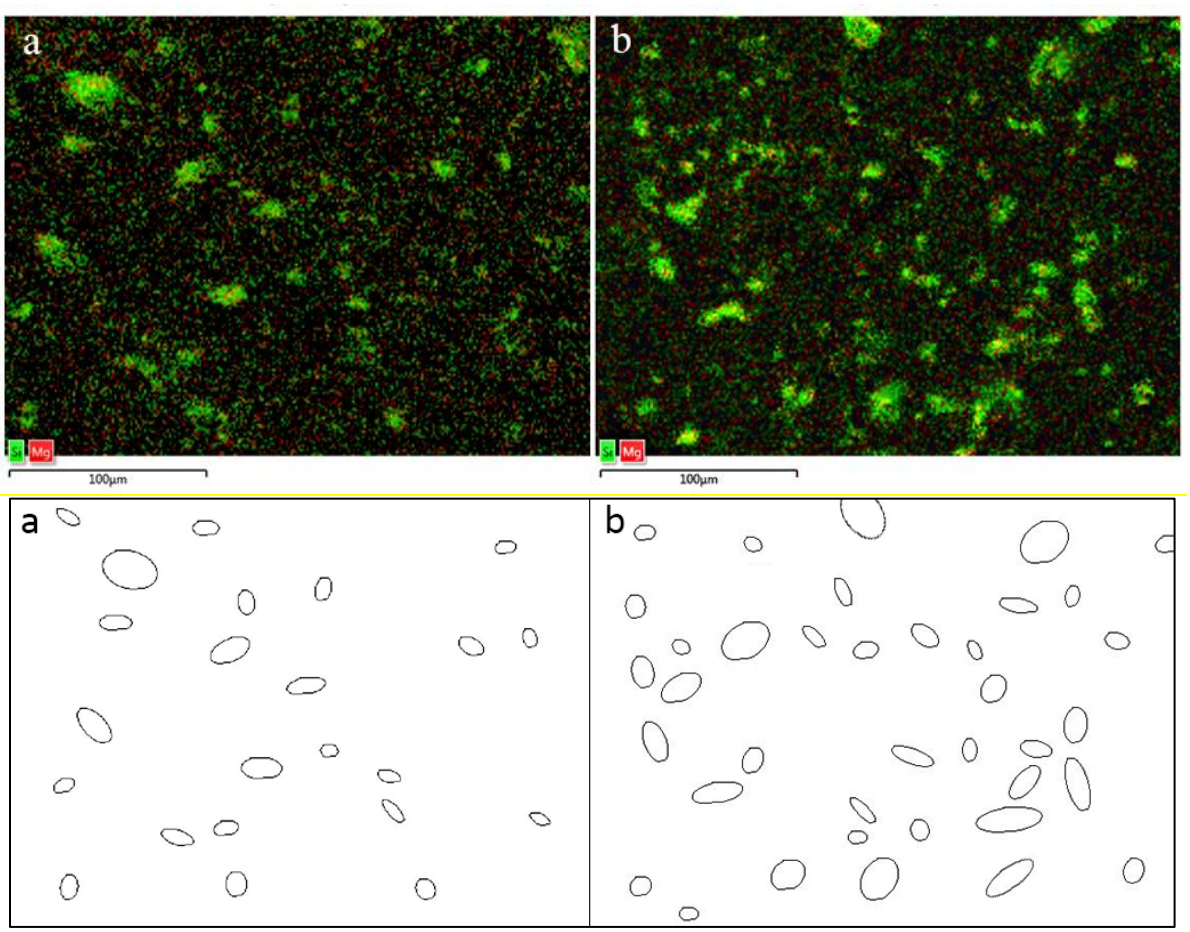

Figure 8. Top: Elemental maps of SEM-EDX images of BMI nanocomposites (a) BMI-B40$_{2.5b}$ and (b) BMI-B40$_{5b}$ showing the distribution of silicon and magnesium atoms in the nanoclay. Bottom: Illustrations of particle dispersion in BMI matrix with (a) 2.5 wt% and (b) 5 wt% nanoclay analysed by Image J analysis software. Nanoclay pieces were simplified as ellipses with different sizes.

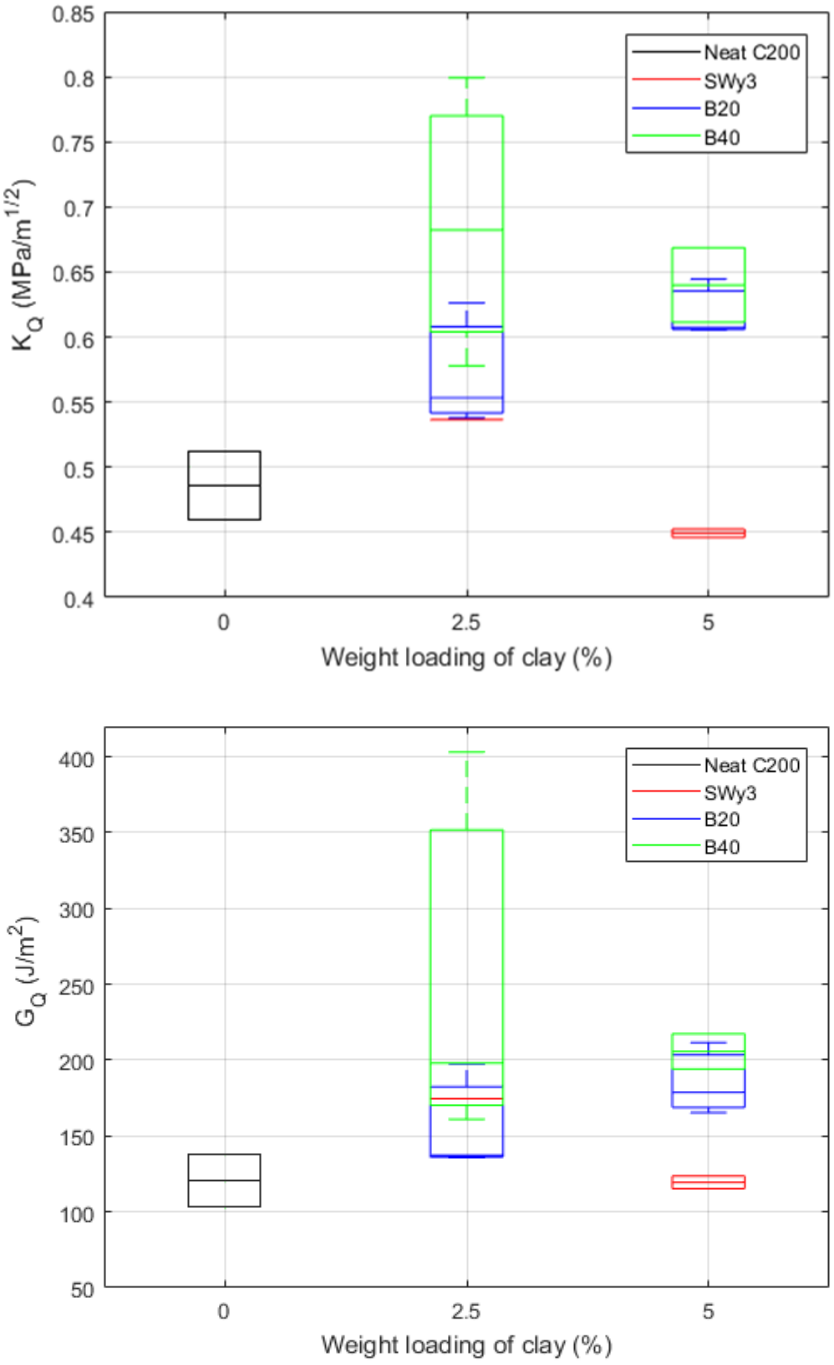

Figure 9. Effect of various nanoclays on K_Q (top) and G_Q (bottom) values for Compimide 200 as a function of clay loading (*N.B.*, all samples were cured using the following schedule: 180 ˚C (3 hours) + 200 ˚C (3 hours)).

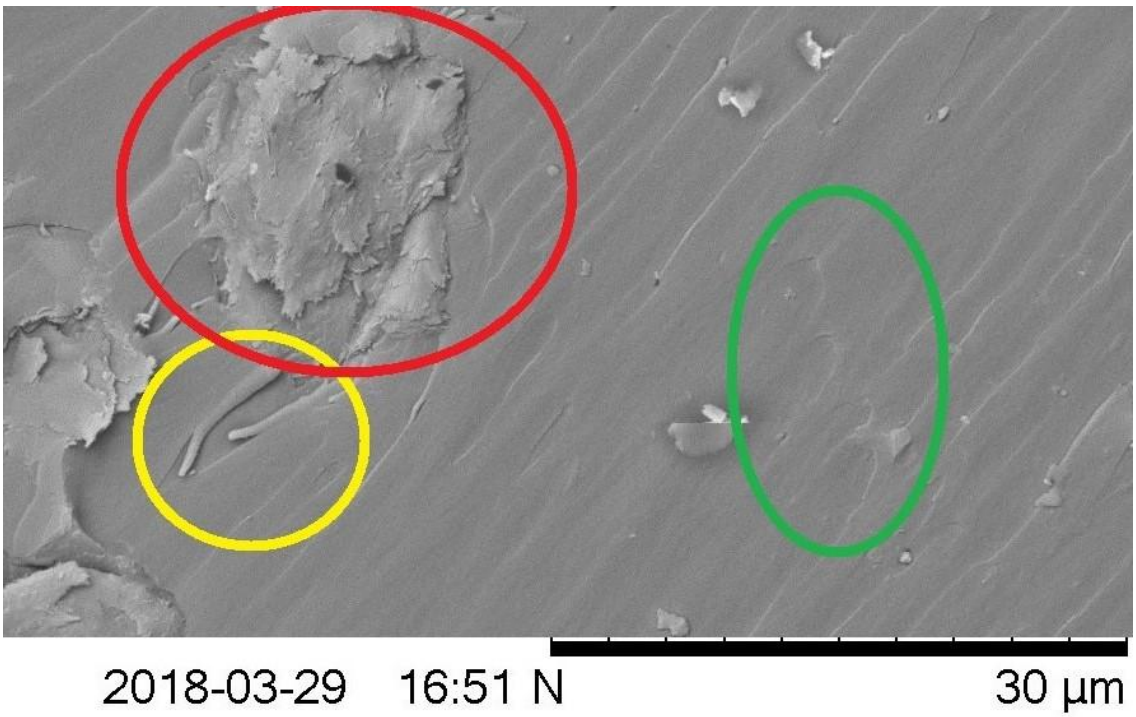

Figure 10. SEM image of a representative toughened sample (BMI-B40$_{5b}$). The highlighted features are a parabola (green circle), ribbon (yellow circle), and a wrenched clay tactoid (red circle).

References

[1] R.J. Iredale, C. Ward, I. Hamerton
Modern advances in bismaleimide resin technology: A 21st century perspective on the chemistry of addition polyimides

Prog. Polym. Sci. 69 (2017) pp. 1-21

[2] S. Kumar, C.P.R. Nair, R. Sadhana, K.N. Nina
Benzoxazine–bismaleimide blends: Curing and thermal properties
Euro. Polym. J. 43 (2007) 5084-5096

[3] A. Chandramohan, A. Shanavas, G. Arunkumar, M. Alagar
Thermal and morphological properties of octa(maleimidophenyl)silsesquioxane (OMPS)-reinforced polybenzoxazine hybrid nanocomposites
Int. J. Polym. Anal. Charact. 18 (2013) pp. 269-279

[4] J.T. Gotro, B.K. Appelt
Characterization of a bis-maleimide triazine resin for multilayer printed circuit boards
IBM J. Res. Dev. 32 (1988) pp. 616-625

[5] G. Liang, Z. Zhang, J. Yang, X. Wang
BMI based composites with low dielectric loss
Polym. Bull. 59 (2007) pp. 269-278

[6] S.B. Driscoll, T.C. Walton
Adhesion and characterization of prepreg processable polyimides
SAMPE J. 23 (1987) p 9

[7] D. Rakutt, E. Fitzer, H.D. Stenzenberger
The fracture toughness and morphology spectrum of bismaleimide-poly(ether imide) moulding compounds
High Perf. Polym. 2 (1990) pp. 133-147

[8] A. Gu, G. Liang
High performance bismaleimide resins modified by novel allyl compounds based on epoxy resins
Polym. Plast. Technol. Eng. 36 (1997) pp. 681-694

[9] L. Yang, Y. Cheng, B. Xia, C. Fang
Structure, mechanical and thermal properties of BMI/E-44/CNTs ternary composites via amination method
J. Mater. Sci. Technol. 33 (2017) pp. 1187-1194

[10] A. Thabet, Y.A. Mobarak, M. Bakry
A review of nano-fillers on industrial polymers and their characteristics
J. Eng. Sci. Assiut University 9 (2011) pp. 77-403

[11] K. Majdzadeh-Ardakani, A.H. Navarchian, F. Sadegh
Optimization of mechanical properties of thermoplastic starch/clay nanocomposites
Carbohydrate Polym. 79 (2010) pp. 547-554

[12] A.C. de Leon, Q. Chen, N.B. Palaganas, J.O. Palaganas, J. Manapat, R.C. Advincuka
High performance polymer nanocomposites for additive manufacturing applications
React. Func. Polym. 103 (2016) pp. 141-155

[13] H.M. Park, W.K. Lee, C.Y. Park, W.J. Cho, C.S. Ha
Environmentally friendly polymer hybrids Part I. Mechanical, thermal, and barrier properties of thermoplastic starch/clay nanocomposites
J. Mater. Sci. 38 (2003) pp. 909-915

[14] A.S. Giroto, A. de Campos, E.I. Pereira, T.S. Ribeiro, J.M. Marconcini, C. Ribeiro
Photoprotective effect of starch/montmorillonite composites on ultraviolet-induced degradation of herbicides
React. Func. Polym. 93 (2015) pp. 156-162

[15] Y. Zheng, Y. Zheng
Study on sepiolite-reinforced polymeric nanocomposites
J. Appl. Polym. Sci. 99 (2006) pp. 2163-2166

[16] J.V. Crivello
Polyaspartimides: condensation of aromatic diamines and bismaleimide compounds
J. Polym. Sci. Part A: Polym. Chem. 11 (1973) pp. 1185-1200

[17] R.W. Lusignea, J.L. Racich, A.C. Harvey, R.R. Chandy
Multiaxially oriented thermotropic polymer substrate for printed wire board
U.S. Patent 4975312 (1990)

[18] M.J. Nanjan, K. Sivaraj
Synthesis and characterization of certain new poly(bisimide)s. Part I
J. Polym. Sci. Part A: Polym. Chem. 27 (1989) pp. 375-388

[19] X. Liu, Y. Yu, S. Li

Viscoelastic phase separation in polyethersulfone modified bismaleimide resin
Euro. Polym. J. 42 (2005) pp. 835-842

[20] T.A. Bullions, A.C. Loos, J.E. McGrath
Advanced composites manufactured via dry powder prepregging
Proceedings of the International Conference on Composite Materials (1999) p. 12

[21] Compimide Bismaleimides, Compimide 200 Product Data Sheet, Evonik, http://root.evonik.com/en/products/search-products/pages/product-details.aspx?pid=12022&pfsearch=C&pfcmd=letter (accessed 22 August 2017)

[22] ASTM Standard D5054
Standard Test Methods for Plane-Strain Fracture Toughness and Strain Energy Release Rate for Plastic Materials
ASTM International, West Conshohocknen, PA (2007)

[23 P. Phiriyawirut, R. Magaraphan, H. Ishida
Preparation and characterization of polybenzoxazine-clay immiscible nanocomposite Mater. Res. Innov. 4 (2001) pp. 187-196

[24] S. Nagendiran, C.K. Chozhan, M. Alagar, I. Hamerton
Inorganic/organic hybrid nanocomposites involving OMMT clay and cyanate ester-siloxane-modified epoxy resin: Thermal, dielectric and morphological properties
High Perf. Polym. 20 (2008) pp. 323-347

[25] C.K. Chozhan, C. Chandramohan, M. Alagar
Surface modified clay reinforced silicon incorporated epoxy hybrid nanocomposites: thermal, mechanical, and morphological properties
Polymers from Renewable Resources. 2018, doi.org/10.1177/204124791800900101

[26] G. Wu, Y. Cheng, K. Wang, Y. Wang, A. Feng
Fabrication and characterization of OMMt/BMI/CE composites with low dielectric properties and high thermal stability for electronic packaging
J. Mater. Sci.: Mater. Electron. 27 (2016) pp. 5592–5599

[27] A.M. Jalali, F.A. Taromi, M. Atai, L. Solhi
Effect of reaction conditions on silanisation of sepiolite nanoparticles
J. Exper. Nanosci. 11 (2016) pp. 1171-1183

[28] Z.X. Zhang, J.S. van Duijneveldt,
Isotropic-nematic phase transition of nonaqueous suspensions of natural clay rods
J. Chem. Phys. 124 (2006) pp. 154910-154917

[29] A. Torró-Pala, J.C. Fernández-García, A.C. Orgilés-Barceló, M.M. Pastor-Blas, J. Martín-Martínez
Structural modification of sepiolite (natural magnesium silicate) by thermal treatment: Effect on the properties of polyurethane adhesives
Internat. J. Adhesion Adhes. 17 (1997) pp. 111-119

[30] The Matrix. Compos World, http://www.compositesworld.com/articles/the-matrix-2016 react-text: 2334 (Accessed July 2016).

[31] J.M. Barton, I. Hamerton, J.B. Rose, D. Warner
The synthesis, characterisation and polymerisation kinetic study of a series of related addition polyimides
High Perf. Polym. 6 (1994) pp. 21-34

[32] K.Y. Lee, D.R. Paul
A model for composites containing three-dimensional ellipsoidal inclusions
Polymer 46 (2005) pp. 9064-9080

[33] C. Di Giulio, M. Gautier, B. Jasse
Fourier transform infrared spectroscopic characterization of aromatic bismaleimide resin cure states
J. Appl. Polym. Sci. 29 (1984) pp. 1771-1779

[34] D.P. Fasce, R.J.J. Williams
Polycondensation of bismaleimides with aromatic diamines
Polym. Bull. 34 (1995) pp. 515-522

[35] A.V. Tungare, G.C. Martin
Analysis of the curing behavior of bismaleimide resins
J. Appl. Polym. Sci. 46 (1992) pp. 1125-1135

[36] J.G. Williams
Fracture mechanics of polymers
Polym. Eng. Sci. 17 (1977) pp. 144-149

[37] M.U. Alvi, S. Zulfiqar, C.T. Yavuz, H.-S. Kweon, M.I. Sarwar
Nanostructure and mechanical properties of aromatic polyamide and reactive organoclay nanocomposites
Mater. Chem. Phys. 147 (2014) pp. 636-643

[38] A.A. Azeez, K.Y. Rhee, S.J. Park, D. Hui
Epoxy-clay nanocomposites: processing, properties, and applications – a review
Composites Part B: Engineering 45 (2013) pp. 308-320

[39] E.S. Greenhalgh
Failure Analysis and Fractography of Polymer Composites, Woodhead Publishers: Cambridge (2009)

[40] C.V. Opelt, L.A. Coelho
Reinforcement and toughening mechanisms in polymer nanocomposites – Reinforcement effectiveness and nanoclay nanocomposites
Mater. Chem. Phys. 169 (2016) pp. 179-185